

Supporting Information

Perovskite Na-conducting battery electrolytes developed from analogous $\text{Li}_{3x}\text{La}_{2/3-x}\text{TiO}_3$ (LLTO): chemo-mechanical and defect engineering

Yu-Ying Lin^{1,3}, William J. Gustafson^{2,3}, Shannon E. Murray^{1,3}, Daniel P. Shoemaker^{1,3}, Elif
Ertekin^{2,3}, Jessica A. Krogstad^{1,3,*}, Nicola H. Perry^{1,3,*}

¹ *Department of Materials Science and Engineering, University of Illinois at Urbana-Champaign, IL, USA*

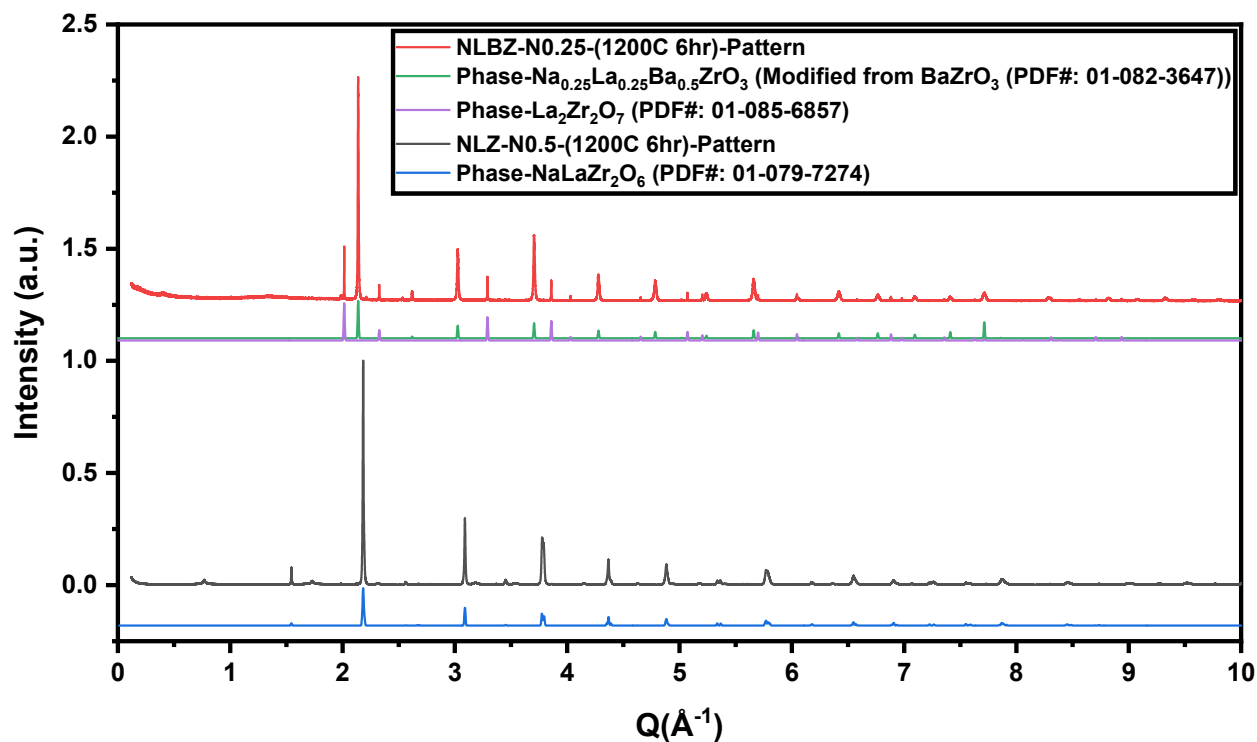
² *Department of Mechanical Science and Engineering, University of Illinois at Urbana-Champaign, IL, USA*

³ *Materials Research Laboratory, University of Illinois at Urbana-Champaign, IL, USA*

* Corresponding authors' emails: jakrogst@illinois.edu, nhperry@illinois.edu

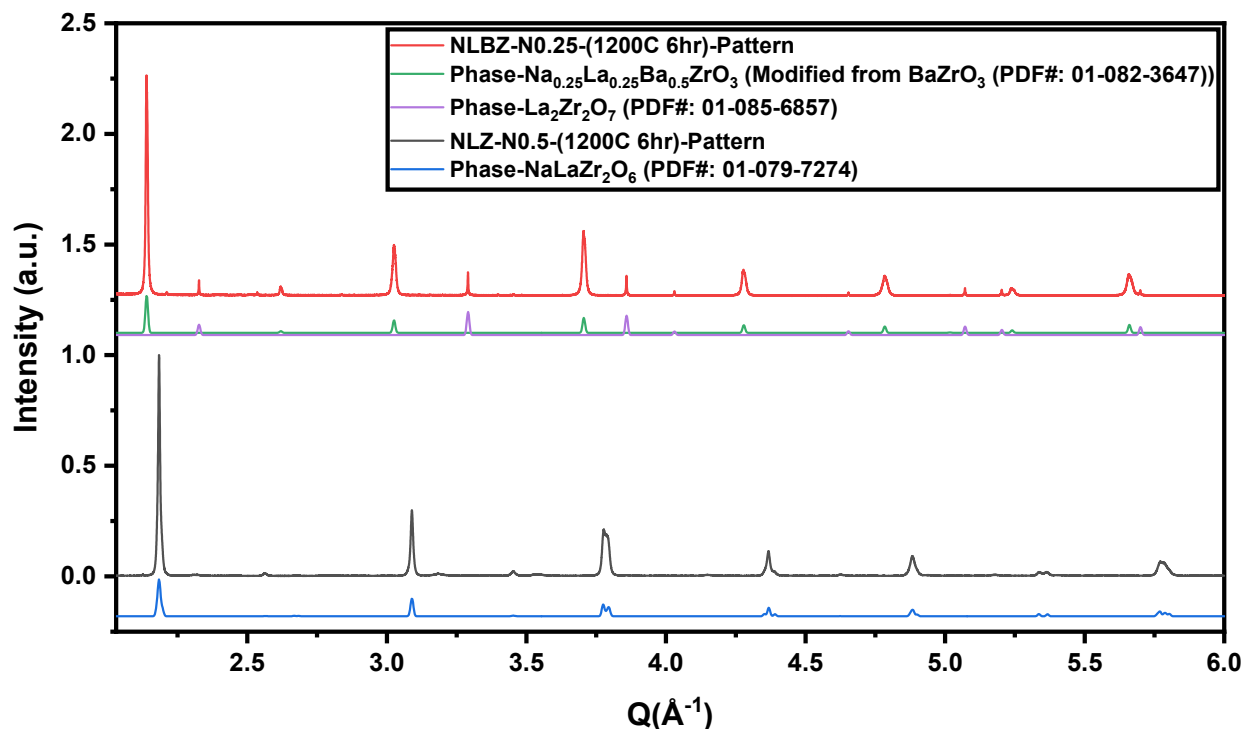
1 1 Synchrotron XRD data for NLZ-N0.5-(1200C 6hr) and NLBZ-N0.25-
2 (1200C 6hr)

3 High-resolution synchrotron powder diffraction data were collected using the rapid access program
4 of beamline 11-BM at the Advanced Photon Source (APS), Argonne National Laboratory with a
5 wavelength of 0.458 Å on NLZ-N0.5-(1200C 6hr) and NLBZ-N0.25-(1200C 6hr). (step size: 0.001°, time
6 per step: 1 second). Analysis of our synchrotron data (Figure S1 and Figure S2), including Rietveld
7 refinement as described in the main manuscript, suggests that $\text{Na}_{0.25}\text{La}_{0.25}\text{Ba}_{0.5}\text{ZrO}_3$ was in a cubic
8 perovskite phase, whereas $\text{Na}_{0.5}\text{La}_{0.5}\text{ZrO}_3$ was orthorhombic with more peak splitting.^{1,2} For visual
9 comparison in the figures, a simulated pattern of $\text{Na}_{0.25}\text{La}_{0.25}\text{Ba}_{0.5}\text{ZrO}_3$ consistent with the analyzed cubic
10 structure, was generated from a modified cif file of cubic BaZrO_3 (PDF#: 01-082-3647) by partially
11 substituting Ba with Na and La according to the stoichiometry. Calculated XRD patterns of observed phases
12 are derived from Powder Diffraction Files (PDF) from International Centre for Diffraction Data (ICDD)
13 database.³



14

15 Figure S1: XRD patterns of NLZ-N0.5-(1200C 6hr) and NLBZ-N0.25-(1200C 6hr) from synchrotron radiation (wavelength=0.458
16 Å), and calculated XRD profiles from ICDD³ for the observed phases.³ R_{wp} values are 17.32% and 12.87% for NLZ-N0.5-(1200C
17 6hr) and NLBZ-N0.25-(1200C 6hr), respectively. Note that there is an unidentified impurity phase in NLZ-N0.5-(1200C 6hr).



1

2 Figure S2: Zoomed in XRD pattern of NLZ-N0.5-(1200C 6hr) and NLBZ-N0.25-(1200C 6hr) from synchrotron radiation
 3 (wavelength=0.458 Å), and calculated XRD profiles from ICDD³ for the observed phases.³

4 2 Measurements with different electrodes

5 Au electrodes deposited by sputtering are very commonly used for cation conductors and were
 6 applied for all the measurements unless otherwise specified. To study the effect of different electrodes, Ag
 7 electrodes and Pt electrodes were also tested. Ag electrodes were applied to see the effect of different
 8 electrodes only on NLZ-N0.5-(1200C 6hr) in dry conditions with $p_{O_2}=1$ atm; Ag paste was painted on the
 9 pellet faces and dried at 300 °C. Total conductivities with Ag electrodes were of the same order of
 10 magnitude, with smaller slopes in the $\ln(\sigma_h T)-1/T$ plot, compared to Au electrodes, suggesting a decrease
 11 in activation energy when the samples were measured with Ag electrodes. Measurements with Ag
 12 electrodes on NLBZ are not reported here as they did not adhere well to NLBZ-N0.25-(1200C 6hr) across
 13 the full measurement temperature range, making the contact area difficult to determine. For the Pt
 14 electrodes, Pt paste was painted on the pellet faces and fired at 850 °C for 2 h on both NLZ-N0.5-(1200C
 15 6hr) and NLBZ-N0.25-(1200C 6hr), and impedance measurements were performed in $p_{O_2}=1$ atm. For both
 16 compositions, conductivities were decreased significantly with Pt electrodes. In addition, slopes in $\ln(\sigma_h T)-$
 17 $1/T$ plot were steeper, suggesting an increase in activation energy when measured with Pt electrodes.
 18 Examination of the samples after elevated temperatures showed that Pt electrodes were very well attached
 19 and no change in the contact area was observed. The Arrhenius plots of porosity corrected total conductivity

1 (σ_h) of NLZ-N0.5-(1200C 6hr) measured with different electrodes can be seen in Figure S3. The total
2 conductivities measured with Au and Ag were similar in magnitude; however, the activation energies were
3 slightly different, with Ag electrodes having a lower activation energy of 0.70 eV compared to Au
4 electrodes with an activation energy of 0.81 eV. On the other hand, the total conductivity measured with Pt
5 was several orders of magnitude lower compared to measurements with Au and Ag. Furthermore, the
6 activation energy was 1.15 eV, much higher compared to Au and Ag.

7 Figure S4 shows the comparison of Nyquist plots of the sample and electrode responses, for
8 different electrodes on NLZ-N0.5-(1200C 6hr), measured in dry, $pO_2=1$ atm at 600 °C from 1 MHz to 1
9 mHz. This temperature was chosen to enable access to the low-frequency response of different electrodes
10 within this frequency range. It can be seen that the electrode responses were very different. For Au
11 electrodes, the electrode response appeared as a 45° straight line, which is a typical behavior for a Warburg
12 impedance element⁴⁻⁶, suggesting that they were completely blocking to sodium ions. In contrast, the
13 response of Ag electrodes deviated from a straight line and were not completely blocking. This may indicate
14 that Ag electrodes allow some sodium ion intercalation into the electrodes or interdiffusion of Ag into the
15 sample. In the case of Pt, the electrodes were also not completely blocking.

16 Sputtered Au electrodes are commonly used for impedance measurements for cation conductors.
17 Au is inert and very unlikely to react with samples. In addition, sputter deposition can be performed at room
18 temperature, so it is less probable that any reaction would occur within the sample or between the sample
19 and the electrodes. An energy dispersive spectroscopy (EDS) cross-sectional line scan also showed no Au
20 signal below 2 μm beneath the surface, as seen in Figure S6. With the sample thickness ranging between
21 1-2 mm, the shallow penetration depth of Au was not significant enough to affect the evaluation of
22 conductivities. As a result, sputtered Au electrodes would have minimum additional contributions when
23 measuring impedance for cation conductors.^{7,8}

24 Ag paste is also widely used when performing impedance measurements. An EDS cross-sectional
25 line scan showed the penetration of Ag to be 5-6 μm (Figure S7), which was also not significant enough to
26 affect the geometry when calculating conductivity. Ag ions are small in radius and potentially mobile,
27 therefore changing the impedance measurement results. Ag ions have been shown to be able to move and
28 modify transport properties within the perovskite structure in LLTO.^{9,10} Ag is also known to exhibit
29 relatively fast diffusion along oxide surfaces.^{11,12} Measuring with Ag electrodes from Ag paste could also
30 contribute uncertainty in evaluating the contact area of the electrodes: For the porous NLBZ-N0.25-(1200C
31 6hr) samples, Ag paste delaminated over time; this degradation was also observed visibly after a few other
32 measurements where edges of the electrodes were no longer attached, reducing the effective electrode area.

1 The delamination of Ag pastes resulted in sharp drops in conductivities during the measurement process
2 (these data were not used). In contrast, sputtered Au electrodes were inert, stable, and well attached.

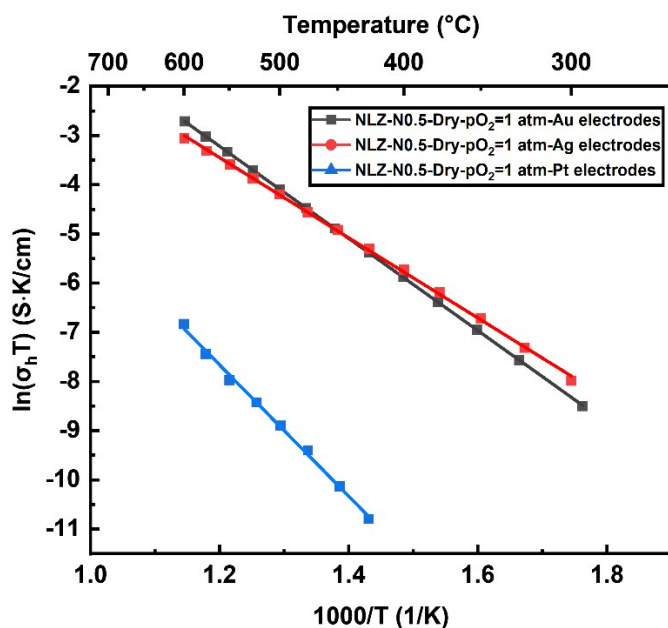
3 Pt paste is another widely used electrode, as Pt is not observed to diffuse into the sample to the
4 same extent as Ag.^{13,14} However, it was observed that the conductivity was orders of magnitude lower than
5 for Ag or Au, and the activation energy was increased with annealed Pt electrodes for both NLZ-N0.5-
6 (1200C 6hr) and NLBZ-N0.25-(1200C 6hr) samples. Delamination was not observed for Pt electrodes on
7 both samples, and no uncertainty in the evaluation of the contact area is expected. An investigation into the
8 much-altered electrical response is discussed further below.

9 DRT analysis of the impedance response of NLZ-N0.5-(1200C 6hr) with different electrodes was
10 performed to observe the effect of electrodes on the sample response itself as seen in Figure S5. The
11 measurement conditions to be compared here were chosen in order to show the most information on the
12 sample response (i.e., to situate the inverse time constant(s) from the sample itself within the measured
13 frequency range). DRT analysis limited to the sample (high frequency) impedance arc suggests that there
14 is only one process (a single time constant) when using Au electrodes. Here, the Warburg element
15 contribution was barely observed because the measurement frequency (1 MHz-100 mHz) did not reach low
16 enough frequencies to reveal it. At higher temperatures or at lower frequencies, the Warburg impedance
17 element was seen in the impedance spectra. For example, at 500 °C, when the sample is more conductive,
18 a clear Warburg impedance contribution was observed in the range of 1 MHz-100 mHz, as seen in Figure
19 5. In addition, at 600 °C, more Warburg impedance element contribution can be seen in the range of 1
20 MHz-1 mHz in Figure S4.

21 There were two processes (two time constants) with Ag electrodes on highly porous samples,
22 which could have resulted from partial Ag ion interdiffusion (e.g., to a limited depth as suggested by EDS),
23 serving as extra carriers moving within the lattice with a different relaxation time to mobile Na ion hopping.
24 As mentioned previously, Ag is known to exhibit relatively fast diffusion along oxide surfaces.^{11,12}
25 Interestingly, the “two time constants” behavior was only observed for porous samples, NLZ-N0.5-(1200C
26 6hr). As seen in Figure S5, the denser NLZ-N0.5-(SPS+1000C 24hr) only showed one process when
27 measured with Ag electrodes. In addition, the activation energy is the same as that of NLZ-N0.5-(1200C
28 6hr) measured using Au electrodes, as seen in Figure 8 in the main text. This result indicates that Ag
29 interdiffusion was negligible in denser samples when less surface area is exposed, and Ag ions do not act
30 as extra carriers.

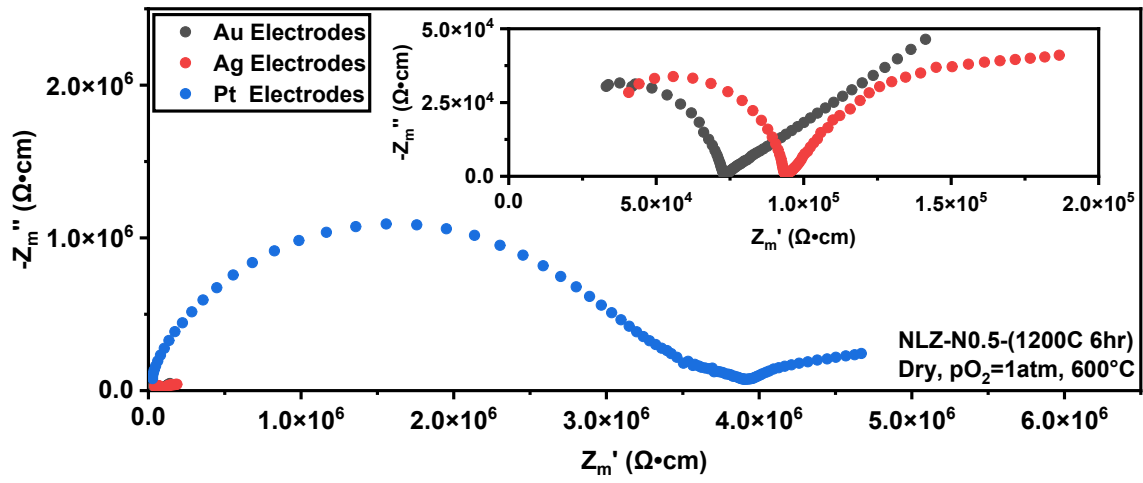
31 In the case of Pt, there were a total of four processes (four time constants) in the high frequency
32 sample impedance arc. With the simultaneous presence of Na, La, Zr, and Pt at the interfaces, chemical

1 reactions forming low conductivity phases could have occurred between the sample and the electrodes
 2 during the high-temperature firing process of the reactive Pt paste at 850 °C^{15,16}, resulting in multiple
 3 processes and decreasing the conductivity significantly. To confirm this suspicion, SEM images were taken
 4 at the cross section, as seen in Figure S8. Interestingly, an additional thin layer of ~3-4 μm was observed
 5 between NLZ and Pt, simultaneously containing La (21.9 atom%), Zr (40.8 atom%), Pt (5.1 atom%), Bi
 6 (32.2 atom%) according to EDS. Pt was not detected beyond 6.35 μm below the surface according to the
 7 EDS line scan. The technical data sheet of the Pt paste from the manufacturer suggests that it contained
 8 other reactive metal oxide to facilitate bonding. From the EDS measurement, we believe that the reactive
 9 metal oxide in the Pt paste contained Bi. In addition, sequential XRD scans were performed with the Pt
 10 layer gradually removed in order to identify any additional phase formation across the interface. Our results
 11 suggest that a pyrochlore phase formed near the surface, whereas only NLZ perovskite phase was detected
 12 in the bulk, as seen in Figure S9. Combining the XRD results with SEM/EDS analysis, we believe that Bi
 13 in the Pt paste reacted with NLZ to form an interphase layer containing (La,Bi)₂Zr₂O₇-pyrochlore phase
 14 that is blocking, significantly reducing the measured conductivity values. Overall, it is likely that such
 15 surface chemistry change during Pt paste firing process led to the multiple time constants and lowered the
 16 measured conductivity values.



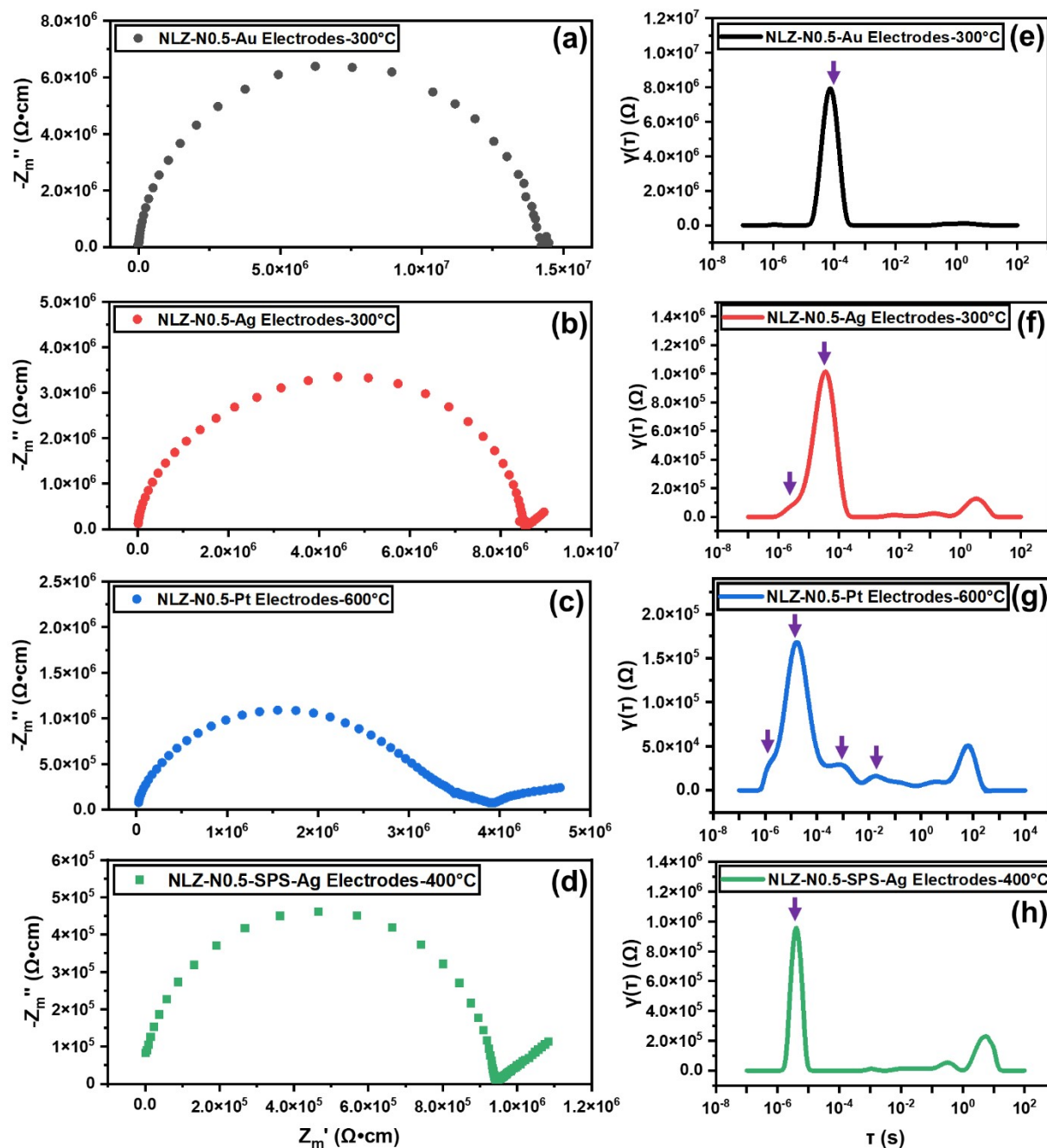
17

18 Figure S3: Arrhenius plots of porosity corrected total conductivity (σ_h) NLZ-N0.5-(1200C 6hr) measured with different electrodes
 19 under dry, $pO_2 = 1 \text{ atm}$ gas environment.



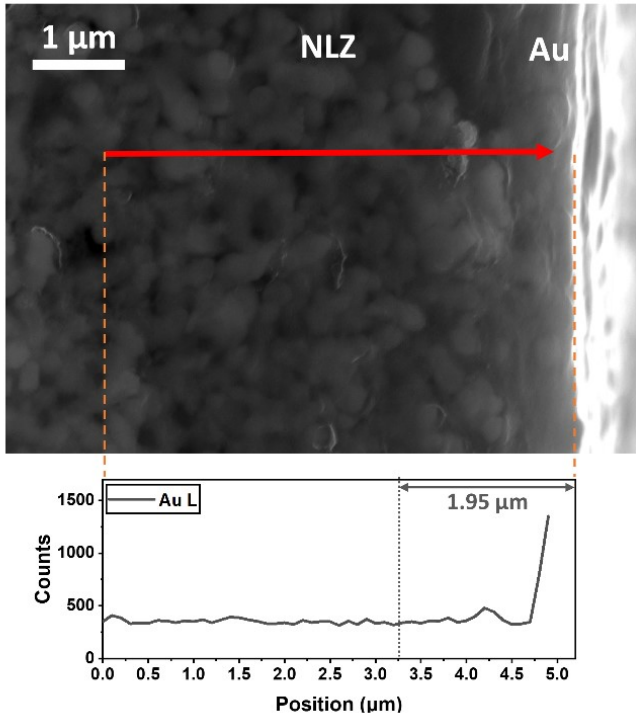
1

2 Figure S4: Nyquist plots of NLZ-N0.5-(1200C 6hr) measured with different electrodes under dry, $pO_2=1$ atm gas environment at
 3 600°C . Inset: Zoomed-in view on responses for Au and Ag electrodes. Z_m' and Z_m'' are respectively the real and imaginary part
 4 of the impedance that is geometry corrected and not porosity corrected.



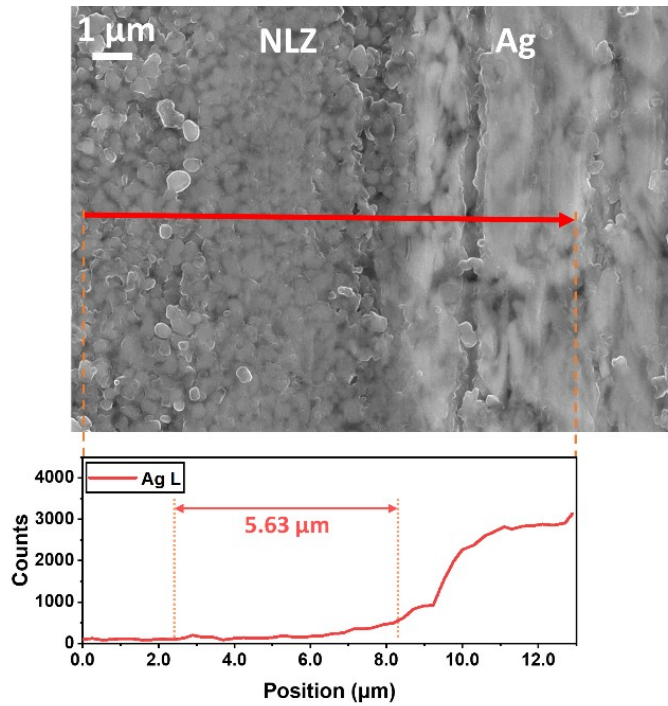
1

2 Figure S5: Nyquist plots and DRT analysis of NLZ-N0.5-(1200C 6hr) and NLZ-N0.5-(SPS+1000C 24hr) measured with different
 3 electrodes (In dry, $pO_2 = 1\text{atm}$ gas environment). (a) Nyquist plot of NLZ-N0.5-(1200C 6hr) measured with Au electrodes,
 4 (b) Nyquist plot of NLZ-N0.5-(1200C 6hr) measured with Ag electrodes, (c) Nyquist plot of NLZ-N0.5-(1200C 6hr) measured with
 5 Pt electrodes, (d) Nyquist plot of NLZ-N0.5-(SPS+1000C 24hr) measured with Ag electrodes, (e) DRT analysis for measurement of
 6 NLZ-N0.5-(1200C 6hr) with Au electrodes, (f) DRT analysis for measurement of NLZ-N0.5-(1200C 6hr) with Ag electrodes, (g) DRT
 7 analysis of measurement for NLZ-N0.5-(1200C 6hr) with Pt electrodes, (h) DRT analysis of measurement for NLZ-N0.5-
 8 (SPS+1000C 24hr) with Ag electrodes. (Peaks in DRT plots are marked with green arrows to indicate various processes.) In
 9 (a)(b)(c)(d), Z_m' and Z_m'' are respectively the real and imaginary part of the impedance that is geometry corrected and not porosity
 10 corrected. In (e)(f)(g)(h), $\gamma(\tau)$ is the distribution function of relaxation times, τ is the relaxation time.



1

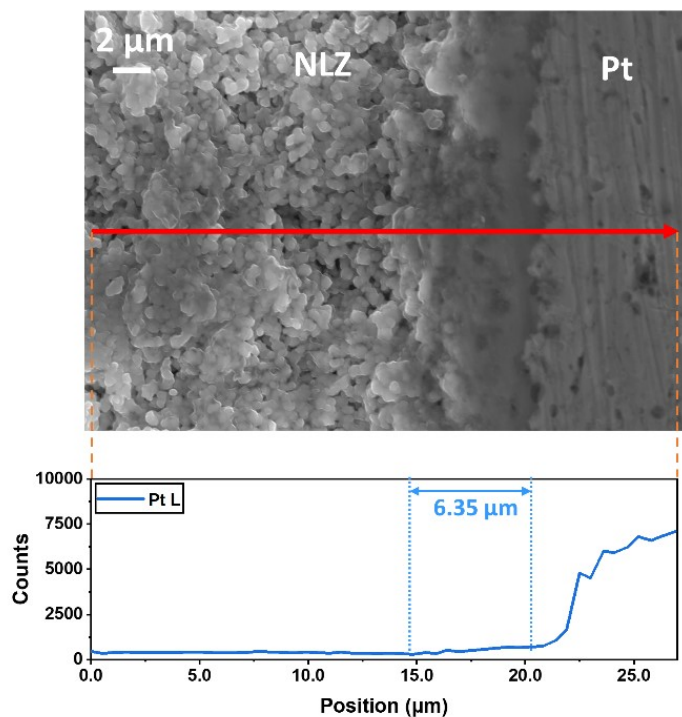
2 Figure S6: Cross section SEM image and EDS line scan on NLZ-N0.5-(1200C 6hr) with sputtered Au. The 1.95 μm corresponds
 3 to the maximum depth Au L peaks were detected beneath the surface of NLZ. Below 1.95 μm, all Au L counts were contributed by
 4 EDS background signal.



5

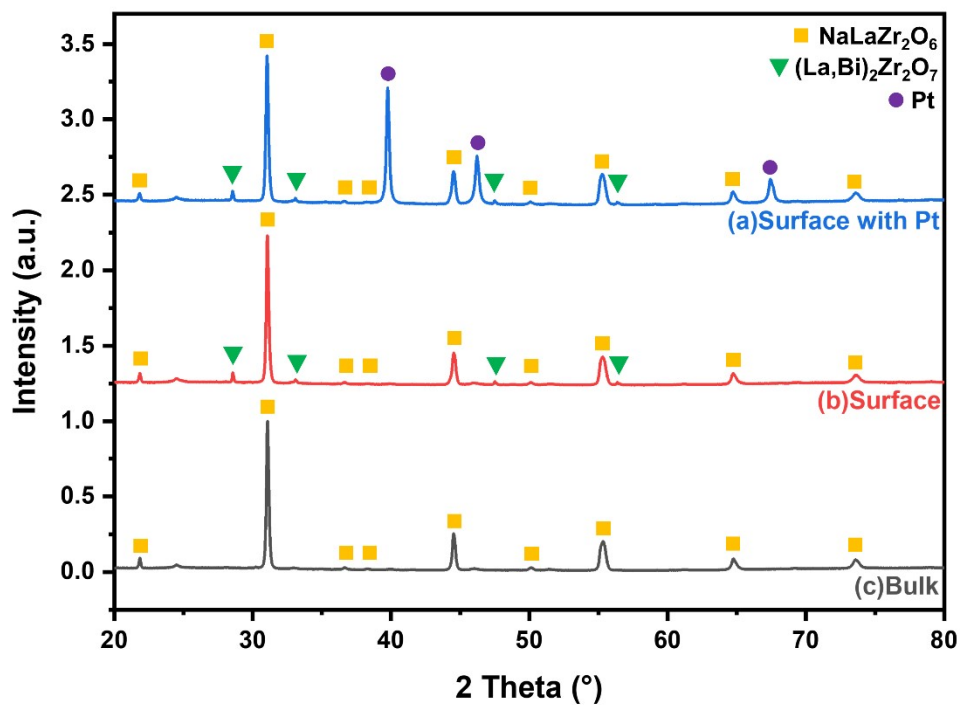
6 Figure S7: Cross section SEM image and EDS line scan on NLZ-N0.5-(1200C 6hr) with Ag paste as electrodes. The 5.63 μm
 7 corresponds to the maximum depth Ag L peaks were detected beneath the surface of NLZ. Below 5.63 μm, all Ag L counts were
 8 contributed by EDS background signal.

1



2

3 Figure S8: Cross section SEM image and EDS line scan on NLZ-N0.5-(1200C 6hr) with Pt paste as electrodes. The 6.53 μm
 4 corresponds to the maximum depth Pt L peaks were detected beneath the surface of NLZ. Below 6.53 μm, all Pt L counts were
 5 contributed by EDS background signal.



6

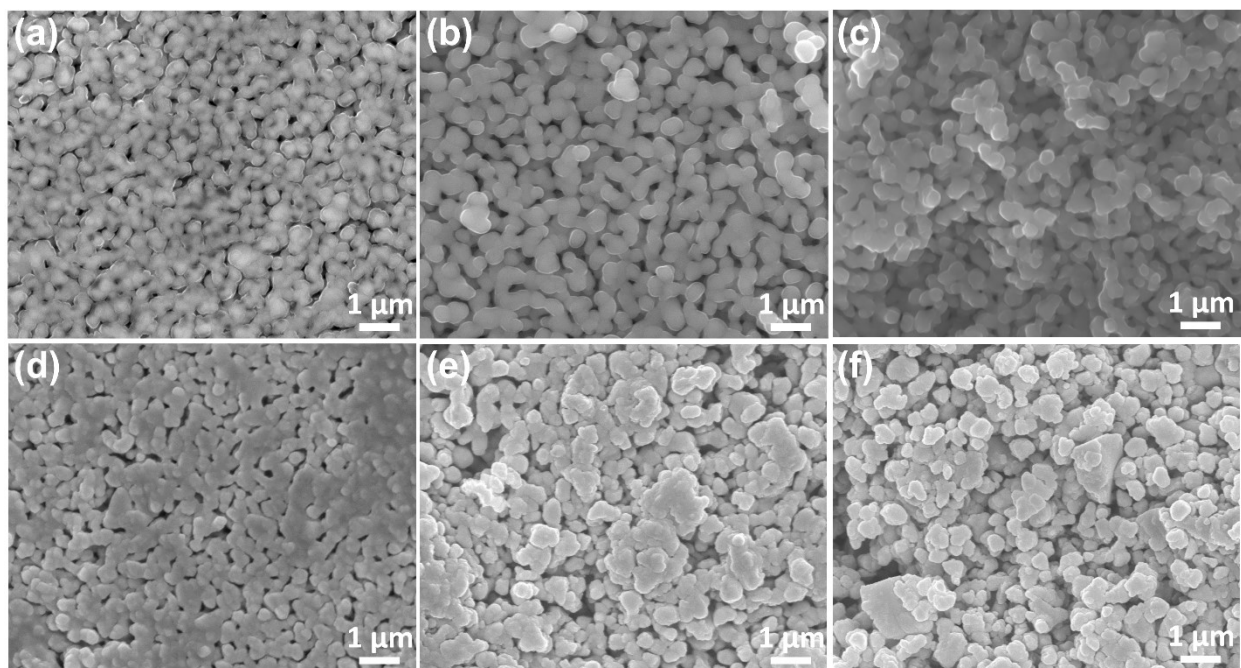
7 Figure S9: XRD patterns of NLZ-N0.5-(1200C 6hr) with Pt paste as electrodes. Pt layer were gradually removed before each scan.
 8 (a) Surface with Pt: XRD scan taken while a thin layer of Pt still remaining on NLZ, (b) Surface: XRD scan taken after the Pt layer
 9 was removed, (c) Bulk: XRD scan taken after the Pt layer and 200-300 μm of NLZ were removed from the surface.

1 3 Transference numbers of different species

2 As mentioned in Sec. 3.2 in the main text, the total conductivities were contributed by sodium ions,
3 oxygen ions, holes, and electrons in dry environments. Total conductivities for both NLZ-N0.5-(1200C
4 6hr) and NLBZ-N0.25-(1200C 6hr) were independent of pO_2 indicating that t_{elec} were negligible for both
5 compositions. To evaluate t_{Na} , DC polarization measurements^{17,18} were performed. With NLZ and NLBZ
6 being oxides, the contribution of oxygen-ion transport cannot be ignored. Therefore, Au was also sputtered
7 onto a yttria stabilized zirconia (YSZ) pellet, a known fast oxygen ion conductor, to examine whether Au
8 electrodes would block oxide-ion transport during DC polarization measurements. YSZ was kept porous
9 with a density of 57.76% in order to mimic the porosity of NLZ-N0.5-(1200C 6hr) and NLBZ-N0.25-
10 (1200C 6hr) as well as the microstructure of sputtered Au electrodes on them. SEM images of both the
11 samples and sputtered Au electrode surfaces can be seen in Figure S10 with both the samples and the
12 electrodes being porous. DC polarization measurements were first performed on YSZ with an applied
13 voltage of 0.3 V. The current density response with respect to time is shown in Figure 7 (c) in the main text.
14 The current density of YSZ was almost invariant with respect to time, suggesting that the sputtered Au
15 electrodes were non-blocking for oxygen; at this temperature, oxygen can be reduced on one electrode and
16 oxidized on the other as the oxide ions move through the sample in a steady-state situation.

17 Au electrodes were blocking for Na ions. The same experiments were then performed on NLZ-
18 N0.5-(1200C 6hr) and NLBZ-N0.25-(1200C 6hr) as seen in Figure 7 (a)(b) in the main text. The current
19 density decays quickly with respect to time; when it reached a steady-state value, $I_{initial}/I_{final}$ was calculated
20 to be 0.0325 and 0.0224, respectively. With porous sputtered Au electrodes being reversible to the transport
21 of oxygen ions and electronic species, the loss of current density at equilibrium can be attributed to only
22 Na ion transport, with the Na ion transference number (t_{Na}) calculated to be 0.9675 and 0.9776, respectively.
23 The application of higher voltage for DC polarization measurements also showed similar results.

24 In summary, with conductivity being independent of pO_2 and the current density decaying in DC
25 polarization measurements, NLZ-N0.5-(1200C 6hr) and NLBZ-N0.25-(1200C 6hr) are predominantly Na
26 ion conductors, with negligible t_{elec} and low t_O .



1

2 *Figure S10: SEM images of YSZ, NLZ, NLBZ and the surfaces of sputtered Au electrodes: (a)YSZ-(1200C 6hr) surface, (b)NLZ-*
 3 *N0.5-(1200C 6hr) surface, (c)NLBZ-N0.25-(1200C 6hr) surface, (d)YSZ-(1200C 6hr) sputtered with Au, (e)NLZ-N0.5-(1200C 6hr)*
 4 *sputtered with Au, (f)NLBZ-N0.25-(1200C 6hr) sputtered with Au.*

5

6

7

8

9

10

11

12

13

14

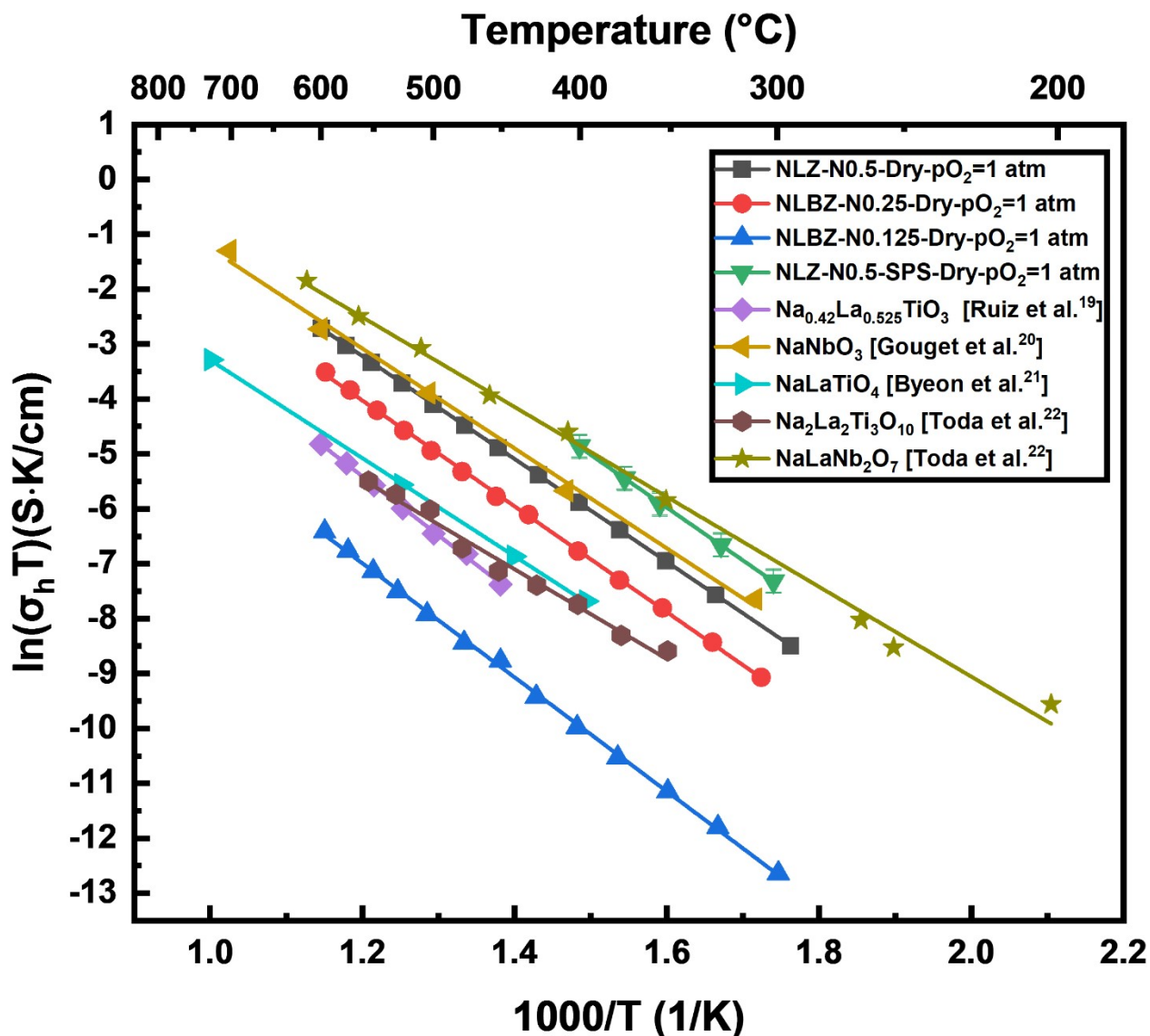
15

16

17

1 4 Comparison Among Reported Perovskite Na-ion Conductors

2 Figure S11 shows the conductivities of NLZ and NLBZ in this work as compared to other
 3 perovskite Na-ion conductors (including RP phases) reported in literature.



4

5 Figure S11: Arrhenius plots of porosity corrected total conductivity (σ_h) of NLZ-N0.5-(1200C 6hr), NLBZ-N0.25-(1200C 6hr),
 6 NLBZ-N0.125-(1200C 6hr) in dry $pO_2=1$ atm environment. Conductivities of $Na_{0.42}La_{0.525}TiO_3$ (Ruiz et al.¹⁹) and $NaNbO_3$ (Gouget
 7 et al.²⁰) are shown here for comparison. Conductivities of Ruddlesden-Popper perovskites $NaLaTiO_4$ (Byeon et al.²¹), $Na_2La_2Ti_3O_{10}$
 8 (Toda et al.²²), $NaLaNb_2O_7$ (Toda et al.²²) are also plotted here for comparison. Note that 12% of the conductivity of $NaNbO_3$
 9 shown here is contributed by O^{2-} .²⁰

1 5 Porosity Corrected Relative Permittivity Calculation

2 As mentioned in Sec. 2.2 in the main text, the impedance spectra were analyzed by equivalent
 3 circuit fitting with a (RQ) circuit because of the single high-frequency arc behavior, as seen in Figure 5.
 4 The measured capacitance (C_m) was first calculated from the measured resistance (R_m), the measured
 5 constant phase element parameter Q_m and the measured constant phase element parameter n_m using Eq.
 6 (S1):

$$7 \quad C_m = \frac{(Q_m R_m)^{\frac{1}{n_m}}}{R_m} \quad (S1)$$

8 Assuming the Bruggeman symmetric medium theory²³⁻²⁵ for spherical pores still holds, the porosity
 9 corrected resistance (R_h) can be calculated from R_m and the volume fraction of the porosity (f) using Eq.
 10 (S2):

$$11 \quad R_h = R_m \left[1 - \frac{3}{2}f \right] \quad (S2)$$

12 Assuming the time constant (τ) remains constant regardless of the porosity, Eq. (S3) should hold:

$$13 \quad \tau = R_m \times C_m = R_h \times C_h = \left(R_m \left[1 - \frac{3}{2}f \right] \right) \times (C_h) \quad (S3)$$

14 where C_h is the porosity-corrected capacitance. As a result, C_h can be calculated using Eq. (S4):

$$15 \quad C_h = \frac{\tau}{R_m \left[1 - \frac{3}{2}f \right]} = \frac{R_m \times C_m}{\left(R_m \left[1 - \frac{3}{2}f \right] \right)} = \frac{C_m}{\left[1 - \frac{3}{2}f \right]} \quad (S4)$$

16 Lastly, the porosity-corrected relative permittivity (ϵ_r) of NLZ and NLBZ can be calculated using Eq
 17 (S5):

$$18 \quad \epsilon_r = \frac{C_h \times d}{\epsilon_0 \times A} = \frac{(Q_m R_m)^{\frac{1}{n_m}} \times d}{R_m \times \left[1 - \frac{3}{2}f \right] \times \epsilon_0 \times A} \quad (S5)$$

19 where d is the distance between electrodes, and A is the area of the electrode, ϵ_0 is the vacuum permittivity. ϵ_r
 20 for NLZ and NLBZ were calculated using the procedures mentioned above for impedance spectra measured

1 between 300 °C-600 °C in dry environments using Au electrodes, which were fitted with a single (RQ).
2 Examples of impedance spectra used to obtain the permittivities can be seen in Figure 5 and Figure S5(a).

3

4

5

6 6 References

- 7 1 M. C. Knapp and P. M. Woodward, *J. Solid State Chem.*, 2006, **179**, 1076–1085.
- 8 2 S. García-Martín, E. Urones-Garrote, M. C. Knapp, G. King and P. M. Woodward, *MRS Proc.*, 2008,
9 **1148**, 1148-PP15-05.
- 10 3 S. Gates-Rector and T. Blanton, *Powder Diffr.*, 2019, **34**, 352–360.
- 11 4 E. Warburg, *Ann. der Phys. und Chemie*, 1899, **303**, 493–499.
- 12 5 J. Huang, *Electrochim. Acta*, 2018, **281**, 170–188.
- 13 6 A. I. Zia and S. C. Mukhopadhyay, eds. A. I. Zia and S. C. Mukhopadhyay, Springer International
14 Publishing, Cham, 2016, pp. 21–37.
- 15 7 A. Mei, Q.-H. Jiang, Y.-H. Lin and C.-W. Nan, *J. Alloys Compd.*, 2009, **486**, 871–875.
- 16 8 J. Wang, X.-P. Jiang, X.-L. Wei, H. Yang and X.-D. Shen, *J. Alloys Compd.*, 2010, **497**, 295–299.
- 17 9 O. Bohnke, C. Bohnke, J. Ould Sid’Ahmed, M. P. Crosnier-Lopez, H. Duroy, F. Le Berre and J. L.
18 Fourquet, *Chem. Mater.*, 2001, **13**, 1593–1599.
- 19 10 K. P. Abhilash, P. C. Selvin, B. Nalini, P. Nithyadharseni and B. C. Pillai, *Ceram. Int.*, 2013, **39**,
20 947–952.
- 21 11 G. Barcaro and A. Fortunelli, *New J. Phys.*, 2007, **9**, 22–22.
- 22 12 R. Ferrando and A. Fortunelli, *J. Phys. Condens. Matter*, 2009, **21**, 264001.
- 23 13 F. Yang, M. Li, L. Li, P. Wu, E. Pradal-Velázquez and D. C. Sinclair, *J. Mater. Chem. A*, 2017, **5**,
24 21658–21662.
- 25 14 S. E. Murray, T. J. Jensen, S. S. Sulekar, Y. Lin, N. H. Perry and D. P. Shoemaker, *J. Am. Ceram.*
26 *Soc.*, 2019, **102**, 7210–7216.
- 27 15 M. J. Davis, M. D. Smith and H.-C. zur Loye, *Inorg. Chem.*, 2003, **42**, 6980–6982.
- 28 16 T. J. Hansen, R. B. Macquart, M. D. Smith and H.-C. zur Loye, *Solid State Sci.*, 2007, **9**, 785–791.
- 29 17 S. Lunghammer, D. Prutsch, S. Breuer, D. Rettenwander, I. Hanzu, Q. Ma, F. Tietz and H. M. R.
30 Wilkening, *Sci. Rep.*, 2018, **8**, 11970.
- 31 18 K. Kataoka, H. Nagata and J. Akimoto, *Sci. Rep.*, 2018, **8**, 9965.
- 32 19 A. I. Ruiz, M. L. López, C. Pico and M. L. Veiga, *J. Solid State Chem.*, 2002, **163**, 472–478.

- 1 20 G. Gouget, F. Mauvy, U.-C. Chung, S. Fourcade, M. Duttine, M.-D. Braida, T. Le Mercier and A.
2 Demourgues, *Adv. Funct. Mater.*, 2020, **30**, 1909254.
- 3 21 S.-H. Byeon, K. Park and M. Itoh, *J. Solid State Chem.*, 1996, **121**, 430–436.
- 4 22 K. Toda, Y. Kameo, M. Fujimoto and M. Sato, *J. Ceram. Soc. Japan*, 1994, **102**, 737–741.
- 5 23 D. A. G. Bruggeman, *Ann. Phys.*, 1935, **416**, 636–664.
- 6 24 D. S. McLachlan, M. Blaszkiewicz and R. E. Newnham, *J. Am. Ceram. Soc.*, 1990, **73**, 2187–2203.
- 7 25 W. Pabst and E. Gregorová, *J. Eur. Ceram. Soc.*, 2014, **34**, 2757–2766.